THE ASTROPHYSICAL JOURNAL, 488:488–498, 1997 October 10
© 1997. The American Astronomical Society. All rights reserved. Printed in U.S.A.

CORONAL MAGNETOGRAPHY OF A SOLAR ACTIVE REGION USING COORDINATED SERTS AND VLA OBSERVATIONS

JEFFREY W. BROSIUS,[1] JOSEPH M. DAVILA, AND ROGER J. THOMAS
Laboratory for Astronomy and Solar Physics, Code 682, NASA/Goddard Space Flight Center, Greenbelt, MD 20771

AND

STEPHEN M. WHITE
Astronomy Program, University of Maryland, College Park, MD 20742
Received 1996 December 2; accepted 1997 May 13

ABSTRACT

We observed NOAA region 7563 simultaneously with Goddard Space Flight Center's Solar EUV Rocket Telescope and Spectrograph (SERTS) and with the Very Large Array (VLA) on 1993 August 17. SERTS obtained spectra in the 280–420 Å wavelength range, and images in the lines of Mg IX λ368.1, Fe XV λ284.1, and Fe XVI λ335.4. The VLA obtained microwave images at 20 and 6 cm wavelengths. The microwave emission depends upon the coronal temperature, density, column emission measure, and magnetic field; therefore, the coronal magnetic field can be derived when all of these other quantities are measured. Here we demonstrate this approach by using the SERTS data to derive all the relevant plasma parameters and then fitting the radio observations to a magnetic field model in order to determine the magnetic field structure.

We used the method of Monsignori-Fossi & Landini and the coronal elemental abundances of Feldman et al. to derive the differential emission measure (DEM) curve for region 7563 from numerous EUV emission lines in spatially averaged SERTS spectra. A similar curve was estimated for each point (i.e., each pixel or each spatial location) in the two-dimensional region by scaling the average DEM curve with corresponding pixel intensities in the Mg IX, Fe XV, and Fe XVI images. We integrated each such DEM over narrow temperature ranges to obtain the column emission measure (CEM) as a function of temperature, CEM(T). We also obtained electron density measurements from EUV line intensity ratios in the spatially averaged spectrum for several ionization stages of iron. These were used to derive a functional relation between density and temperature, $n_e(T)$.

We derived the temperature dependence of the coronal magnetic field [$B(T)$] at each point in the two-dimensional region by incorporating CEM(T) and $n_e(T)$ into expressions for the thermal bremsstrahlung and the gyroresonance opacities, and varying $B(T)$ so as to minimize the difference between the calculated and the observed microwave intensities. The resulting calculated 20 and 6 cm microwave intensity images reproduce the observed images very well. We found that thermal bremsstrahlung alone is not sufficient to produce the observed microwave intensities: gyroemission is required. Further, contrary to several earlier studies, we found no evidence for cool, absorbing plasma in the solar corona above the active region. The coronal magnetic fields derived with our method typically exceed the coronal fields extrapolated with a simple potential model, suggesting the presence of coronal electric currents. However, in the diminutive sunspot which dominates the 6 cm emission this difference is relatively small, suggesting that the sunspot magnetic field itself is nearly potential. Although we cannot firmly establish the uniqueness of our solution in this particular case, the method is quite powerful and should be repeated with other similar data sets. Variations in the coronal elemental abundances could affect the determination of the microwave emission mechanism(s), introduce evidence for the presence of cool coronal plasma, and alter the strengths of the derived coronal magnetic fields.

Subject headings: Sun: activity — Sun: corona — Sun: magnetic fields — Sun: radio radiation — Sun: UV radiation

1. INTRODUCTION

Solar wind acceleration and coronal heating are widely believed to be driven by magnetic processes. In this paper we describe and apply a method for directly measuring magnetic fields in the Sun's corona above an active region. Our method exploits the dependence of microwave emission upon the coronal magnetic field and is accomplished by using a coordinated set of EUV and microwave observations. The derived two-dimensional coronal magnetic field maps are referred to as *coronal magnetograms*. Although an absolute height scale can only be estimated for the coronal magnetograms in this work, the variation of the field strength with temperature in each image pixel can be derived. Therefore, the coronal magnetographic method described below provides three-dimensional information on the structure of the coronal magnetic field.

Two mechanisms contribute to the microwave emission from nonflaring coronal plasma: thermal bremsstrahlung (free-free) and thermal gyroresonance (cyclotron). Thermal bremsstrahlung emission results from the interaction of unbound electrons with protons, and its intensity depends upon the coronal plasma temperature and column emission

[1] Also Hughes STX Corporation, 4400 Forbes Boulevard, Lanham, MD 20706.

measure. This represents the minimum possible microwave intensity which emanates from the plasma. Thermal gyroemission results from thermal electrons spiraling along coronal magnetic field lines. It is emitted at low harmonics of the local electron gyrofrequency, and its intensity depends upon the coronal density, temperature, and magnetic field. The degree of circular polarization for both emission mechanisms depends upon the coronal magnetic field. The key to measuring coronal magnetic fields is to obtain coronal *plasma* parameters (density, temperature, and emission measure) from observations of optically thin X-ray and/or EUV emission lines (which are insensitive to coronal magnetic fields), and then use these quantities in equations for the thermal bremsstrahlung and gyroresonance opacities so that coronal *magnetic* parameters (field strength and direction) can be obtained from a comparison of observed and "calculated" microwave intensities.

Coordinated microwave and X-ray or EUV observations have been carried out since the *Skylab* era in attempts to garner information about coronal magnetic fields (Kundu, Schmahl, & Gerassimenko 1980; Kundu, Schmahl, & Rao 1981; Pallavicini, Sakurai, & Vaiana 1981; Shibasaki et al. 1983; Webb et al. 1983, 1987; Lang et al. 1987b; Brosius et al. 1992, 1993). Frequently, the observed microwave intensity has been found to be less (by factors of 2–5) than the thermal bremsstrahlung (minimum possible) intensity calculated from the X-ray or EUV observations. This has been interpreted as evidence for the presence of relatively cool absorbing plasma along the line of sight between the observer and the microwave-emitting region (Holman 1986; Webb et al. 1987; Lang et al. 1987a; Nitta et al. 1991; Brosius, Holman, & Schmelz 1991; Brosius et al. 1992; Schmelz et al. 1992, 1994) or as evidence for scattering by a turbulent spectrum of fluctuations in the coronal electron number density (Bastian 1994).

Brosius et al. (1991, 1992) and Schmelz et al. (1992, 1994) adapted the Sakurai (1982) potential field extrapolation code to derive two-dimensional extrapolated magnetograms at specified (sometimes numerous and closely spaced) heights in the corona to aid with the analysis of observations obtained during the 1987 coronal magnetic structures observing campaign (CoMStOC). These *extrapolated* coronal magnetograms, although not "true" coronal magnetograms, were particularly useful for the analysis of the microwave polarization since a treatment of mode coupling in a "quasi-transverse" layer in the coronal magnetic field (e.g., Zheleznyakov 1970; Bandiera 1982) was sometimes necessary. Other key results from CoMStOC include (1) evidence for the presence of cool coronal plasma at some locations, (2) demonstration that potential field extrapolations are sometimes adequate, and other times inadequate (yield field strengths which are too low) to explain the observed microwave emission, and (3) derivation of plasma and magnetic field parameters in individual sunspots and coronal loops.

Other workers (Bogod et al. 1992; Lang et al. 1993) have relied upon similar adaptations of the Sakurai (1982) code to obtain extrapolated coronal magnetograms. They combined these potential models of the solar coronal magnetic field with constant conductive flux models of the solar atmosphere to compute theoretical microwave emission maps for comparison with observations. At some locations their theoretical and observed maps agreed well, demonstrating that the potential extrapolation provided a reasonable approximation of the coronal field at those places. At other locations their theoretical intensities exceeded their observed intensities, suggesting the presence of cool absorbing plasma; at still other locations, their theoretical intensities were less than their observed intensities, indicating a possible role for nonpotential coronal fields (e.g., Lee et al. 1997).

Recently, several authors derived maps of the coronal magnetic field without relying upon potential extrapolations from photospheric longitudinal magnetograms. Brosius et al. (1993) used coordinated SERTS and VLA observations to derive coronal magnetograms in a solar plage area, while Gary & Hurford (1994) used Owens Valley Radio Observatory (OVRO) multiple wavelength observations to derive coronal magnetograms of a solar active region.

Brosius et al. (1993) used 1991 SERTS EUV images in Fe XV λ284.1 and Fe XVI λ335.4 to determine the two-dimensional temperature and emission measure distribution in a solar plage area. (The assumption of an isothermal corona was the greatest shortcoming of that work.) A map of the expected 20 cm thermal bremsstrahlung emission was calculated from the temperature and emission measure maps and found to agree well with the observed emission. This indicated that thermal bremsstrahlung *alone* was responsible for the 20 cm plage emission, and a coronal magnetic field map was derived from the observed 20 cm polarization. The derived coronal magnetogram agreed reasonably well with potential field extrapolations to heights between 5000 and 10,000 km.

Gary & Hurford (1994) acquired OVRO two-dimensional synthesis maps at 22 microwave frequencies to obtain a two-dimensional grid of brightness temperature spectra. They used these spectra to deduce the temperature, emission measure, and dominant emission mechanism at each position. Where gyroemission was found to dominate, the coronal magnetic field was obtained by assuming that either the second or the third harmonic (at the turnover frequency in the spectrum) was optically thick. The selection of the appropriate harmonic was the greatest source of uncertainty in their analysis.

The present work represents a significant step forward in coronal magnetographic techniques from Brosius et al. (1993) and Gary & Hurford (1994). In particular, we account for the nonisothermality of the active region corona by incorporating an emission measure distribution covering the temperature range from 10^5 to 10^7 K for each spatial pixel (each location) in our microwave emission calculations. Further, we use several density-sensitive line intensity ratios from the SERTS observations to determine directly, rather than infer from modeling, the dependence of density upon temperature. We incorporate both thermal bremsstrahlung and thermal gyroemission in order to derive the temperature distribution of the coronal magnetic field which minimizes the differences between the calculated and the observed microwave intensities in each pixel of the two-dimensional images. Knowledge of the density, emission measure, and volume filling factor as functions of temperature provides a means of estimating height as a function of temperature.

The SERTS/VLA coordinated data set provides the most extensive coverage of plasma parameters and multiwavelength microwave emission currently available for a solar active region. In § 2 we describe the observations; in

§ 3 we develop the techniques of coronal magnetography; in § 4 we present our results; in § 5 we discuss our results in light of earlier studies; and in § 6 we summarize our conclusions.

2. OBSERVATIONS

We obtained simultaneous Very Large Array[2] (VLA) microwave images, SERTS EUV spectra and spectroheliograms, and KPNO spectromagnetograph (Jones et al. 1992) photospheric longitudinal magnetograms and He I λ10830 images of NOAA active region 7563 (S10 W15) around 1800 UT on 1993 August 17. The active region was relatively weak. It had three small spots with a total areal coverage of 10 millionths of the visible hemisphere (1993 Solar Geophysical Data) and a maximum photospheric longitudinal magnetic field of $\sim$500 G. The spots in region 7563 did not manifest themselves in the form of intensity depressions in either the hot EUV emission or the *Yohkoh* Soft X-Ray Telescope X-ray emission (see Webb 1981), but at least one of them appears as a weak microwave source in the eastern portion of the region.

2.1. *SERTS*

We used SERTS to obtain a spatially averaged spectrum of NOAA region 7563 in the wavelength range 280–420 Å, and spectroheliograms of the active region in the emission lines of Mg IX λ368.1 (log $T_{max} = 5.98$), Fe XV λ284.1 (log $T_{max} = 6.33$), and Fe XVI λ335.4 (log $T_{max} = 6.43$). T_{max}, the "formation temperature," is the temperature which maximizes the fractional ion abundance in the available ionization equilibrium calculations (Arnaud & Raymond 1992 for Fe ions; Monsignori-Fossi 1992 for Mg).

The SERTS instrument is described by Neupert et al. (1992). Its spectrograph entrance aperture was designed to enable both spectra and spectroheliograms (of different areas) to be obtained simultaneously. Spectra are obtained along a narrow slit which connects two rectangular lobes within which the spectroheliograms are imaged. Because of the relatively small area covered by the rectangular lobes (5×8 arcmin^2), the amount of spectral overlap is greatly reduced from that of earlier EUV spectroheliographs. By adjusting the pointing of the instrument during its flight, both images and spectra can be obtained for the same portion of the Sun. This capability is extremely valuable in the analysis which follows. The spatial resolution is $\sim$5″, and the spectral resolution (instrumental FWHM) is $\sim$55 mÅ.

SERTS was launched on a Terrier-boosted Black Brant rocket from White Sands, New Mexico, at 1800 UT on 1993 August 17. Data were recorded between 100 and 492 s after launch. Brosius et al. (1996) discuss the radiometric calibration of the data obtained during this flight and provide the spatially averaged spectrum of NOAA region 7563 which is used in this work. Brosius et al. (1997) describe the method for coaligning SERTS data with coordinated ground-based observations and develop a background removal algorithm for the spectroheliograms. All SERTS images used in the present paper have been corrected for background emission in this way.

[2] The VLA is a facility of the National Radio Astronomy Observatory, which is operated by Associated Universities, Inc., under cooperative agreement with the National Science Foundation.

Numerous emission lines are available in the SERTS slit spectra. These include lines from the eight ionization stages of iron between Fe X and Fe XVII, as well as lines from other species such as He II, Mg VIII and IX, Si VIII through XI, and Ni XVIII. These lines are formed in widely differing temperature regimes, and thus provide diagnostic capabilities for multithermal plasmas from $\sim 10^5$ to 10^7 K. Brosius et al. (1996) used the differential emission measure (DEM) technique developed by Monsignori-Fossi & Landini (1991, 1995) to derive a DEM curve for region 7563 from the spatially averaged spectrum. The application of this curve to the present work will be described in detail below. Brosius et al. (1996) also obtained numerous density-sensitive line intensity ratios from the active region averaged spectrum, and we use their results here to obtain a functional relation between density and temperature.

2.2. *VLA*

We used the C-configuration VLA to obtain right-hand (R) and left-hand (L) circularly polarized images of region 7563 at 1.465 GHz (20 cm), 5.0 GHz (6 cm), 8.0 GHz (3.7 cm), and 15 GHz (2.0 cm) between 1420 UT and 1820 UT on 1993 August 17. The quality of the data in the highest two frequencies is fairly poor owing to the relative weakness of the region. We therefore restrict our analysis in what follows to the 20 and 6 cm emission. All images were reduced with the conventional CLEAN techniques. The beam sizes at 20 and 6 cm wavelengths were 16″.9 × 14″.5 and 6″.5 × 5″.0, respectively.

We compensated each map for missing background flux by adding an appropriate quiet-Sun background brightness temperature of 1×10^5 K at 20 cm, and $2.5 \pm 0.5 \times 10^4$ K at 6 cm (Zirin, Baumert, & Hurford 1991; White, Gary, & Kundu 1996). This still left some regions of negative flux near the active region, but none within the area which would interfere with our analysis below.

2.3. *KPNO Spectromagnetograph*

We used the KPNO spectromagnetograph to obtain a full-disk He I λ10830 image at 1536 UT, and a full-disk photospheric longitudinal magnetogram at 1438 UT. Both of these were shifted in order to compensate for solar rotation during the time interval between their acquisition and the time of the rocket flight (1800 UT). The spatial resolution of the KPNO data is $\sim$1″.15.

We obtained the absolute pointing of the SERTS spectrograph by coaligning the SERTS He II λ304 images with the He I λ10830 (absorption) image (Brosius et al. 1997). The formal uncertainty on this coalignment is $\sim$7″. Since the absolute pointing of the VLA is known to high accuracy, this procedure enabled us to reliably coalign the SERTS and VLA observations. We used the photospheric longitudinal magnetogram to extrapolate coronal potential magnetic fields (using our adaptation of the Sakurai code) for comparison with the coronal fields derived by the coronal magnetographic method described in this paper.

3. CORONAL MAGNETOGRAPHY

The coronal magnetic field derived in this work is obtained from (1) directly observed quantities, (2) parameters easily calculable from the diectly observed quantities, and (3) several very simple assumptions. Therefore the method that we describe below is one for *measuring* (as

directly as possible), rather than for *extrapolating*, the coronal magnetic field. Implications of our various assumptions are discussed in a separate subsection at the end of this section.

3.1. *General Method*

The general approach is as follows. We assume that temperature increases monotonically with height over the height range of interest and use a scaling law derived from SERTS data to specify the relationship between density and temperature at each spatial pixel and each height within the active region. The DEM along the line of sight through each spatial pixel is determined from the SERTS data, and, in conjunction with the scaling law between n_e and T, this specifies the plasma parameters completely. The contributions of thermal bremsstrahlung to the radio emission at any frequency and in any spatial pixel can now be determined. Any excess of radio flux not consistent with thermal bremsstrahlung is then attributed to gyroresonance emission. In addition to the plasma parameters, one must specify the magnetic field strength, magnetic field scale height, and the angle between the magnetic field and the line of sight in order to calculate gyroresonance emission. In this calculation, we will assume a value for the magnetic scale height and use the radio observations to derive the two remaining parameters by minimizing the difference between the observed and the calculated microwave brightness temperatures. We use temperature as the independent variable, since the relationship between height and magnetic field is only poorly constrained by the data (e.g., White & Kundu 1997).

Thus the coronal magnetographic method employed here yields the temperature distribution of the total magnetic field strength and the orientation of the field with respect to the line of sight for each spatial location in a two-dimensional array. For each spatial location, the solar atmosphere along the line of sight is divided into 21 discrete intervals of uniform temperature such that the hottest plasma is on top, and the temperature decreases monotonically downward. The temperature logarithm ranges from 7.0 to 5.0, in decrements of 0.1 dex. The optical thickness of the ith interval (at any given microwave frequency) is

$$\Delta\tau_i^{X,O} = \Delta\tau_{\mathrm{ff},i}^{X,O} + \Delta\tau_{\mathrm{gr},i}^{X,O} , \tag{1}$$

where $\Delta\tau_{\mathrm{ff},i}^{X,O}$ is the optical thickness of the interval due to the free-free mechanism, $\Delta\tau_{\mathrm{gr},i}^{X,O}$ is the optical thickness of the interval due to the gyroresonance mechanism, and X and O refer to the extraordinary and ordinary modes of electromagnetic wave propagation. The free-free optical thickness is given by

$$\Delta\tau_{\mathrm{ff},i}^{X,O} = \frac{9.786 \times 10^{-21}(\mathrm{CEM}_i)\ln(\alpha/\nu)}{n_{\nu,i}\, T_i^{1.5}(\nu \mp \nu_{B,i}\cos\theta_i)^2} , \tag{2}$$

where $\alpha = 47T_i$ for temperatures above 3.16×10^5 K and $\alpha = 4.954 \times 10^{-2} T_i^{1.5}$ otherwise; CEM_i is the column emission measure of the ith interval in cm^{-5}, T_i is the electron temperature of the ith interval in K, ν is the observation frequency in GHz, $n_{\nu,i}$ is the index of refraction in the ith interval for the frequency ν (see Ginzburg 1964; Ramaty 1969), $\nu_{B,i}$ is the gyrofrequency in GHz, θ_i is the angle between the magnetic field and the line of sight, and the minus sign refers to the extraordinary mode while the plus sign refers to the ordinary mode. The gyroresonance optical thickness is given by

$$\Delta\tau_{\mathrm{gr},i}^{X,O} = 0.052\,\frac{S^{2S}}{2^{S+1}S!}\, n_{e,i}\nu^{-1}L_B \times (1.77 \times 10^{-10}T_i)^{S-1}(1 \pm \cos\theta_i)^2 \sin^{2S-2}\theta_i , \tag{3}$$

where S is the harmonic number (e.g., 2, 3, 4, ...), $n_{e,i}$ is the electron density in the ith interval, L_B is the magnetic scale height $B/\nabla B$ in units of 10^9 cm (which we take here to be unity; see Brosius et al. 1992), and the plus sign refers to the X-mode while the minus sign refers to the O-mode. $\Delta\tau_{\mathrm{gr},i}^{X,O}$ is nonzero only for intervals in which the observation frequency is an integral multiple (harmonic) of the local electron gyrofrequency. Since radio emission is strongly attenuated for heights below the plasma level, where the index of refraction becomes imaginary, first harmonic emission is generally not seen.

The microwave emission from each discrete height interval in the solar atmosphere passes through the overlying intervals prior to exiting the atmosphere and is modified by the total opacity of those layers. The total optical depth of each interval is given by the sum of the optical thicknesses of all of the overlying intervals

$$\tau_i^{X,O} = \sum_{j=1}^{i} \Delta\tau_{j-1}^{X,O} , \tag{4}$$

and $\tau_0^{X,O} = 0$. Thus the contribution to the total brightness temperature (in kelvins) from the ith interval is

$$\Delta T_{B,i}^{X,O} = T_i[1 - \exp(-\Delta\tau_i^{X,O})]\exp(-\tau_i^{X,O}) . \tag{5}$$

The total microwave brightness temperature is calculated by summing over the contributions from all of the discrete, constant-temperature–emitting intervals at their corresponding optical depths:

$$T_B^{X,O} = \sum \Delta T_{B,i}^{X,O} . \tag{6}$$

The microwave intensity (in kelvins) is given by

$$I = (T_B^X + T_B^O)/2 . \tag{7}$$

The magnetic field strength as a function of temperature was calculated for each spatial location (each line of sight) by minimizing the difference between the calculated and the observed intensity for that line of sight, for observations at both 1.465 and 5.0 GHz. Two-dimensional maps of the microwave intensity were then constructed for each observing frequency from the calculated minimum-difference intensities. Results, shown in Figure 1, will be discussed below.

3.2. *Application of SERTS Data*

SERTS data were used to obtain numerical values of the density and column emission measure in the above equations. It should be emphasized that our SERTS images encompass the temperature range which is most important for contributing to the 20 cm microwave emission (1–2.5×10^6 K), and that our density diagnostics are also most reliable for a smaller but comparable temperature range.

Brosius et al. (1996) derived electron densities with various line intensity ratios from a spatially averaged SERTS spectrum of NOAA region 7563. We used their average log n_e (cm^{-3}) values for Fe XIII (9.66 ± 0.49, log $T_{\max} = 6.20$), Fe XIV (9.58 ± 0.14, log $T_{\max} = 6.27$), and

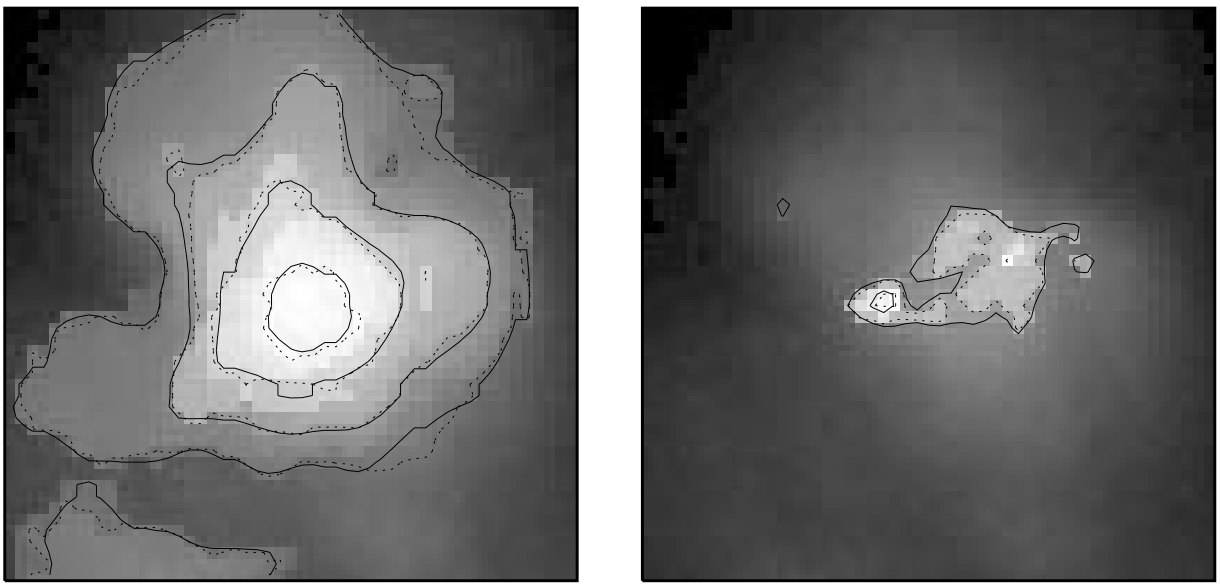

FIG. 1.—*Left:* calculated 20 cm intensity image, with calculated (*dotted*) and observed (*solid*) contours of 0.25, 0.5, 1.0, 1.5 × 10^6 K. *Right:* calculated 6 cm intensity image, with contours of 1.0 and 2.5 × 10^5 K. Note the excellent agreement between the calculated and the observed contours in each image. Solar north is up, and west is to the right. The image size is 225″ × 225″.

Fe XV (9.41 ± 0.22, log $T_{max} = 6.33$) to obtain the following linear relationship between log n_e and log T:

$$\log n_e = 21.466 - 1.9015 \log T \, . \quad (8)$$

Although strictly speaking this relation applies only to the narrow temperature range $6.20 \leq \log T \leq 6.33$, we assume that it is applicable over the entire temperature range from log $T = 5.0$ to 7.0. Equation (8) yields reasonable extrapolated density logarithms of 11.95 at log $T = 5.0$ and 8.15 at log $T = 7.0$.

Brosius et al. (1996) used the method of Monsignori-Fossi & Landini (1991, 1995) and the coronal elemental abundances of Feldman et al. (1992) to derive the *differential emission measure* (DEM, in cm^{-5} K^{-1}) for NOAA region 7563 from numerous emission lines in spatially averaged active region spectra. This curve provides the average temperature distribution of the emitting plasma in the active region. The DEM can be integrated over small, discrete temperature intervals in order to derive the *column emission measure* (CEM, in cm^{-5}) as a function of temperature. The latter is needed for each spatial location in the two-dimensional active region area in order to accurately compute maps of the thermal bremsstrahlung emission. However, since the number of spectroheliograms at specific EUV wavelengths is relatively small, the method of Monsignori-Fossi & Landini (1991, 1995) cannot be directly applied to the individual spatial pixels in the two-dimensional images. Instead, we estimated the DEM for each spatial pixel in the two-dimensional images by scaling the spatially averaged DEM curve (of Brosius et al. 1996) by the intensities in the corresponding pixels of the Mg IX λ368.1 (log $T_{max} = 5.98$), Fe XV λ284.1 (log $T_{max} = 6.33$), and Fe XVI λ335.4 (log $T_{max} = 6.43$) images. For $5.0 \leq \log T \leq 6.0$, we multiplied the spatially averaged DEM values by the ratio of the Mg IX λ368.1 individual pixel intensity to the spatially averaged Mg IX λ368.1 intensity. Similarly, for $6.4 \leq \log T \leq 7.0$, we multiplied the spatially averaged DEM values by the ratio of the Fe XVI λ335.4 individual pixel intensity to the spatially averaged intensity. For log $T = 6.3$ we used a similar ratio of Fe XV intensities. For intermediate log T values we interpolated. We integrated the scaled DEM for each spatial pixel to obtain the CEM and inserted the latter into equation (2) in order to calculate the thermal bremsstrahlung optical thickness of each discrete temperature interval.

3.3. *Application of VLA Data*

The final step in determining the temperature dependence of the coronal magnetic field $B(T)$ in each pixel of the two-dimensional images was a pixel-by-pixel comparison of the calculated and the observed 20 and 6 cm microwave intensities.

The VLA images were rescaled to match the SERTS image scale (4.″41 $pixel^{-1}$) in order to facilitate the pixel-by-pixel comparison of the observed and the calculated microwave intensities. We restricted our analysis of the coronal magnetic field to pixels in which the 20 cm intensity exceeded 2.4 × 10^5 K; the 6 cm emission was incorporated in the analysis only for pixels in which the 6 cm intensity exceeded 1 × 10^5 K. This enabled us to avoid the noisiest portions of the microwave observations.

For each spatial pixel, we characterized the coronal magnetic field with three parameters: (1) the total field strength in the hottest (uppermost) temperature interval, (2) the factor by which the field strength increased from interval to interval (the field increased monotonically with depth or, in other words, with decreasing temperature in the atmosphere), and (3) the (depth-invariant) angle between the field and the line of sight. With these three parameters, the coronal magnetic field is specified in each discrete temperature interval, i.e., we know $B(T)$. For computational purposes, we considered an individual harmonic to be located within a given temperature interval if the magnetic field strengths in the two adjacent intervals bracketed the field strength appropriate for that harmonic.

We calculated the 20 cm microwave intensity for numerous combinations of values of the above three parameters. The combination which yielded the minimum difference

between the calculated and the observed 20 cm intensities was taken as the best solution for the given pixel. If the 6 cm emission was significant as defined above, we adjusted the magnetic field (strength and angle) in the relevant portion of the atmosphere in order to accommodate *both* the 6 and the 20 cm emission. Since the 6 cm intensities are so low, this meant adjusting magnetic parameters (2) and (3) only in the cooler portions of the atmosphere, below the levels which contribute to the 20 cm emission. Thus two different values for the angle between the field and the line of sight were obtained for areas in which signficant emission in two different microwave frequencies was observed. It should be emphasized that these calculations were performed for each spatial location (each pixel) individually and that the technique is essentially one of trial and error.

We determined whether the longitudinal (line-of-sight) component of the coronal magnetic field was directed inward (toward the Sun) or outward (toward the observer) by attributing the greater of the observed R and L component to X-mode emission. If the R component corresponded to X-mode emission, the field is directed outward. If the L component corresponded to X-mode emission, the field is directed inward. The orientation of the magnetic field in the derived coronal magnetograms was found to generally agree with that of the underlying photospheric field.

3.4. *Limitations on the Coronal Magnetographic Method*

In applying our coronal magnetographic method we are limited by the nature of the data available, which forces us to make a number of simplifying assumptions. Here we discuss these assumptions, along with their effects upon our results.

First, our adopted density-temperature relation (eq, [8]) was derived with density-sensitive line intensity ratios from only three different ions covering a relatively narrow temperature range ($6.20 \leq \log T \leq 6.33$). Strictly speaking, equation (8) is valid only over that narrow range, but we applied it to the entire range $5.0 \leq \log T \leq 7.0$. While the validity of this assumption cannot easily be tested, we believe that the use of observations to determine n_e and T *as well as* the differential emission measure represents an advance on previous calculations of this type, and we point out that the density diagnostics are most reliable for a temperature range which is comparable to the 20 cm brightness temperatures of the active region core. Equation (8) places the plasma level for an unmagnetized plasma (where the observation frequency is equal to the plasma frequency $\nu_p = 8.98 \times 10^{-6} n_e^{1/2}$, with ν_p in GHz and n_e in cm^{-3}) at $\log T = 5.81$ for 1.465 GHz emission, and at $\log T = 5.25$ for 5.0 GHz emission. The corresponding temperatures will shift somewhat for the X- and O-modes in the presence of a magnetic field. Emission from plasma cooler than these $\log T$ values will not propagate to the observer. However, based upon the measured brightness temperatures, the active region microwave emission originates in higher temperature plasma anyway. Furthermore, although the densities on which the density-temperature relation is based were derived from line intensities which were averaged over the most active portions of the region, we applied this relation to all locations in the active region and its environs. It is reasonable to do this since we have found (Brosius et al. 1996, 1997) that active region and quiet-Sun densities differ by factors of only about 2. We point out that our adopted density-temperature relation does not affect our determination of the relevant microwave emission mechanism(s): since free-free emission depends directly upon the column emission measure, but only weakly upon the density (through the index of refraction), our finding that thermal bremsstrahlung alone is inadequate to produce the observed microwave emission is independent of the density-temperature relation.

Second, we assumed that the magnetic scale height, L_B, is uniformly (at all spatial locations and for all heights) 1×10^9 cm. We are therefore ignoring any small-scale features in the magnetic field in the corona: for such features we are also limited by the spatial resolution of both radio and EUV data. The assumed value is consistent with those found by Brosius et al. (1992) from potential extrapolations. In the present work it is difficult to derive L_B because we do not have an independent means of determining the *height* dependence from the *temperature* dependence of the derived magnetic field. However, by combining a reasonable value of 0.01 for the volume filling factor (based upon intensity and density measurements for the various emission lines; Falconer 1994; Brosius et al. 1996) with the column emission measure for each atmospheric temperature interval, we can derive the thickness of each discrete temperature interval, and hence the height of any given interval. Using this method, we derived L_B values $\sim 1 \times 10^9$ cm, consistent with our initial assumption.

Third, we have only two radio frequencies available, and thus are only sensitive to very restricted values of the coronal magnetic field. For this reason, we assumed that for any given spatial location the number of different θ values along the line of sight is equal to the number of different microwave frequencies observed at that location. For a spatial location from which no significant 5.0 GHz emission is detected, θ remains constant along the entire line of sight (i.e., it does not vary with temperature or height). For a spatial location from which both 1.465 and 5.0 GHz emission is observed, two different values for θ are derived: one angle is that which is most appropriate for the harmonic which dominates the 1.465 GHz emission, while the other is that which is most appropriate for the harmonic which dominates the 5.0 GHz emission. This assumption could slightly affect the calculated microwave polarization since the actual angles in the free-free and weak (higher harmonic) gyroemission regions may be different from our derived values; however, without high-quality maps at additional microwave frequencies it is not possible to place additional constraints upon the temperature variations of θ. The two microwave observing frequencies employed in this work are far enough apart in frequency that their emission arises from separate portions of the atmosphere; variations of parameters in one does not effect the emission of the other.

Fourth, we assumed that the magnetic field strength increases monotonically with decreasing temperature (with decreasing height). This yields field strengths which become unrealistically large toward the lower levels of the atmosphere ($\log T \sim 5.0$). However, it should be pointed out that these large field strengths occur because parameters in this portion of the atmosphere are relatively unconstrained by the available observations. If we had higher quality, greater frequency microwave observations available (such as may be obtained with the proposed Solar Radio Telescope), we could obtain reliable, realistic field strengths in this portion of the atmosphere. Note that the

microwave emission from these large-field intervals does not contribute to the observed emission since it originates either below the plasma level or below the smallest optically thick harmonic.

Many of the limitations of the calculation presented here are due to inadequate data rather than intrinsic problems in the approach, and we expect improved results to be achieved with more comprehensive data sets which will be available in the future.

4. RESULTS

4.1. *Comparison between Calculated and Observed Microwave Intensity Maps*

We explored the possibility that thermal bremsstrahlung alone could produce the observed 20 cm emission by calculating a map of the free-free 20 cm microwave intensity. Since the coronal magnetic field affects the polarization but not the intensity of the thermal bremsstrahlung emission, we made the reasonable assumption that the field was zero. This yielded a map whose morphology differed noticeably from that of the observed map and the intensities of which were factors ~ 2 less than the observed. This indicates that thermal bremsstrahlung alone is not adequate to produce the observed 20 cm emission. In addition, since the free-free intensities are significantly less than the observed, it demonstrates that an additional mechanism (thermal gyroemission) must contribute to the observed microwave intensity. Although this does not preclude the presence of cool coronal plasma, it certainly does not provide any evidence for the presence of such plasma.

By including both thermal bremsstrahlung and thermal gyroemission, the calculated microwave intensity maps do agree quite well with observations at the two analyzed frequencies. This is shown in Figure 1, where we plot calculated (*dashed*) and observed (*solid*) intensity contours on grayscale images of the 20 and 6 cm calculated intensities. Corresponding intensity contours clearly trace each other very well. Similar agreement between the observed and calculated contours in the left- and right-hand circularly polarized images, not shown here, was also found. Although this agreement clearly indicates that our solution for the coronal magnetic field is a reasonable one, it does not demonstrate that our solution is unique. We expect that the coronal magnetic field would vary somewhat if we included observations at additional microwave frequencies in our analysis. Furthermore, uncertainties on the EUV and microwave intensity measurements, as well as uncertainties on the derived densities and column emission measures, impose limitations upon the uniqueness of any derived solution. Nevertheless, our method is sound and provides the best approach to date of performing coronal magnetography with coordinated microwave and EUV (or X-ray) observations. With high-quality observations at additional microwave frequencies, such as would be available with the Solar Radio Telescope, we could do a more thorough analysis of active region coronal magnetic field structures.

4.2. *Coronal Magnetograms*

Figure 2 shows coronal magnetograms corresponding to heights in which the plasma temperatures are 2×10^6, 1×10^6, and 5×10^5 K. The overall shape of each image resembles that of the 20 cm microwave emission (Fig. 1, *left*) because we restricted our derivation of the coronal magnetic field to areas in which the 20 cm intensity exceeded 2.4×10^5 K. Coronal magnetic field strengths as high as 175 G are found in the 2×10^6 K plasma, 250 G in the 1×10^6 K plasma, and 500 G in the 5×10^5 K plasma. These field strengths are appropriate for 20 cm third harmonic emission, 20 cm second harmonic emission, and 6 cm fourth harmonic emission, respectively. A sunspot source is evident just left of the center of each image; this is the strongest source in the 6 cm intensity map (Fig. 1, *right*).

Figure 3 shows extrapolated coronal potential magnetograms at heights of 10,000, 5000, and 2500 km for comparison with the coronal magnetograms of Figure 2. The maximum field strengths at these heights are 105, 190, and 240 G, respectively. The sunspot source just left of image center is evident in all three frames of this figure. Although there is no reason to expect the images of Figures 2 and 3 to be directly comparable, some structural similarities are evident. For example, the sunspot source is clearly seen in both sets of figures, as is a general elongation of the magnetic structure from southeast to northwest.

We estimated the height variation of the magnetic field for selected lines of sight by calculating the thickness Δl_i of each emitting interval from the density, column emission measure, and estimated filling factor f of the interval: $\Delta l_i = \mathrm{CEM}_i / f n_{e,i}^2$. The height of any given interval was then derived by summing the thicknesses of all the underlying

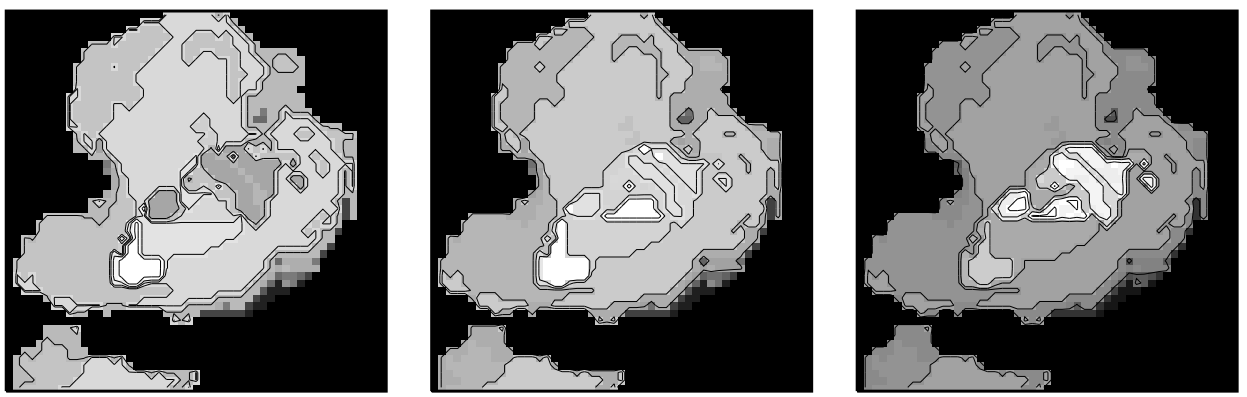

FIG. 2.—Derived coronal magnetograms at (*left*) log $T = 6.3$, (*middle*) log $T = 6.0$, and (*right*) log $T = 5.7$. Contour levels are (*left*) 100, 125, 135, 150, 175, G; (*middle*) 100, 150, 175, 200, 250 G; (*right*) 100, 200, 225, 300, 400, 500 G. The overall shape of the magnetograms is similar to that of Fig. 1 (*left*) because we restricted our derivation of the coronal magnetic field to areas in which the 20 cm microwave intensity exceeded 2.4×10^5 K. Solar north is up, and west is to the right. The image size is $225'' \times 225''$.

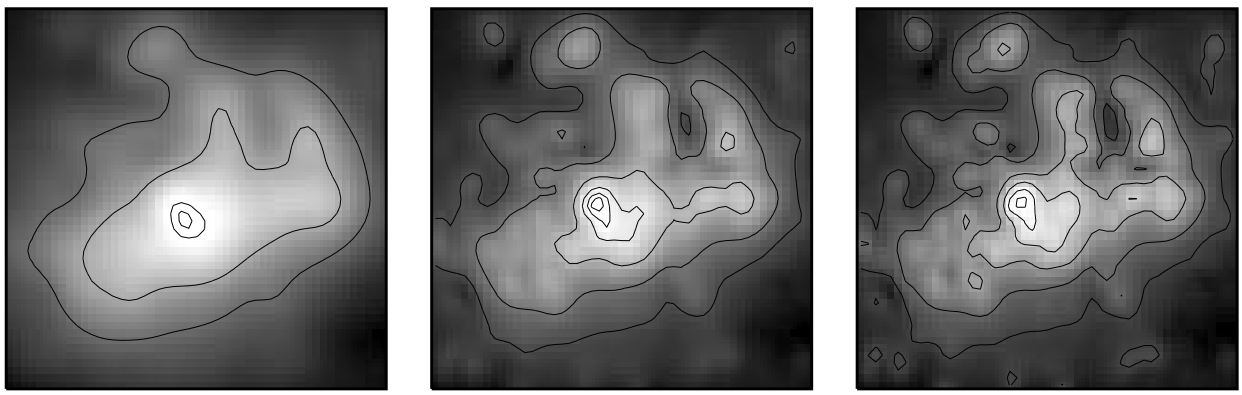

FIG. 3.—Extrapolated coronal potential magnetograms at heights of (*left*) 10,000, (*middle*) 5000, and (*right*) 2500 km. Contour levels are (*left*) 25, 50, 100, 105 G; (*middle*) 25, 50, 100, 150, 175, 190 G; (*right*) 25, 50, 100, 150, 200, 240 G. Solar north is up, and west is to the right. The image size is 225″ × 225″.

intervals. The filling factor must be included because the entire thickness of any given interval is not necessarily filled with plasma at its specified density: only the portion of the interval that emits EUV radiation is filled with plasma at the specified density. Falconer (1994) and Brosius et al. (1996) obtained filling factors between ~ 1 and $\sim 10^{-4}$. In the present work, we found that filling factors ~ 1 yielded very low heights (~ 100 km) for the 10^6 K plasma. We therefore chose an intermediate value of 0.01 for the filling factor in the analysis which follows.

We selected three different lines of sight along which to calculate the height variation of the magnetic field (and temperature) as described above: (1) the 6 cm intensity peak, (2) the 20 cm intensity peak, and (3) a "typical" pixel with a 20 cm intensity of $\sim 1 \times 10^6$ K. The heights of the 1×10^6 K plasma are 5800, 7700, and 7300 km in those three cases, and the corresponding heights of the 2×10^6 K plasma are 14,000, 16,000, and 16,000 km. The height variation of the coronal magnetic field is shown in Figure 4. For comparison, we plot the height variation of the extrapolated potential field at the same locations. The coronal magnetic field derived in this work is clearly greater than the coronal field extrapolated from the potential model. At the 20 cm intensity peak and at the "typical" pixel, our calculated magnetic fields exceed the potential fields by factors of 2 or more. This suggests the presence of field-enhancing coronal electric currents. However, at the 6 cm intensity peak our calculated fields are comparable to the potential fields. Since the 6 cm intensity peak overlies a small sunspot in the active region, this suggests that the small sunspot field is nearly potential. A comparison of the contour levels in Figures 2 and 3 further reveals that the coronal potential fields are generally smaller than the fields derived with our method. For example, the outermost contour in our derived magnetogram of Figure 2 (*center*; log $T = 6.0$) is 100 G, while the first three contours in the extrapolated potential magnetogram of Figure 3 (*center*; height = 5000 km) are 25, 50, and 100 G; field strengths of 100 G are reached only toward the center of this potential magnetogram.

5. DISCUSSION

It is instructive to compare outcomes of the present analysis with those from earlier, similar analyses. Here we discuss the issue of cool coronal plasma in light of coronal elemental abundance measurements and equilibrium ionization fraction computations. This helps us assess the current state of the art of coronal magnetographic techniques and provides insight into possible sources of uncertainty.

All four X-ray/microwave coordinated observing runs from the 1987 Coronal Magnetic Structures Observing Campaign (CoMStOC) provided evidence for the presence of cool coronal plasma ($T \lesssim 5 \times 10^5$ K) (Nitta et al. 1991; Brosius et al. 1991, 1992; Schmelz et al. 1992, 1994) because the *actual* microwave brightness temperatures observed with the VLA were factors of 2 or more smaller than the *expected*

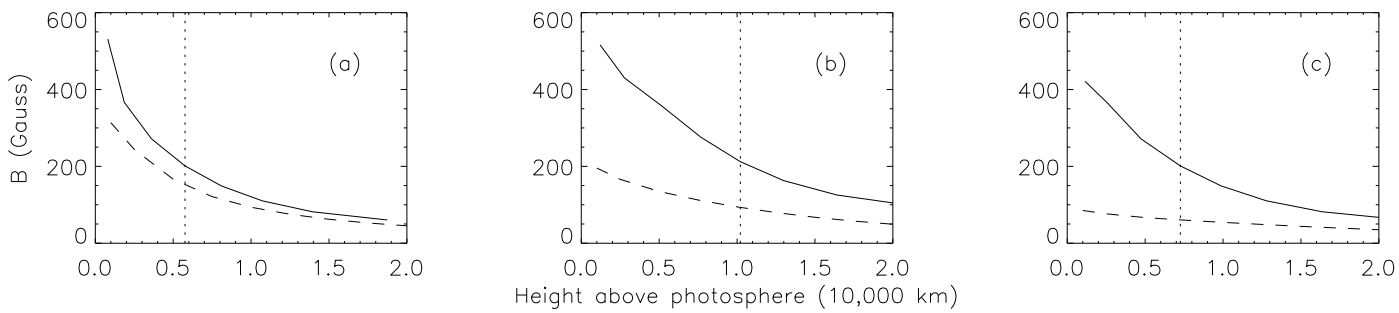

FIG. 4.—Comparison of the height variation of the magnetic field strength derived with our method using a filling factor of 0.01 (*solid*), with that derived from the potential model (*dashed*), at (*a*) the 6 cm intensity peak, (*b*) the 20 cm intensity peak, and (*c*) a "typical" pixel with 20 cm intensity $\sim 1 \times 10^6$ K. The *y*-axis is the field strength in gauss, and the *x*-axis is the height in 10^4 km. For heights from which the contributions to the 20 cm emission are greatest (*vertical dotted lines*), the ratios between our calculated coronal magnetic field strengths and the corresponding extrapolated potential fields are (*a*) 1.32 (*b*) 2.27, and (*c*) 3.33.

microwave brightness temperatures calculated from the *Solar Maximum Mission* (*SMM*) X-Ray Polychromator (XRP) observations. Additional evidence for the presence of cool coronal material, deduced from different types of observations, has been presented by Schmahl & Orrall (1979), Kanno & Suematsu (1982), Bogod et al. (1992), and Gary & Hurford (1994). *SMM*/XRP provided active region intensity images in soft X-ray emission lines from two or more of the O VIII, Ne IX, Fe XVII, Mg XI, and Fe XVIII ions. Image intensity ratios were used to derive maps of the active region coronal temperature, and the temperature maps were combined with the O VIII intensity images to derive column emission measure maps. The coronal elemental abundances of Meyer (1985) and the equilibrium ionization computations of Arnaud & Rothenflug (1985) were used for all of the CoMStOC analyses. Expected microwave brightness temperatures were calculated from the XRP temperature and column emission measure maps under the assumption that only thermal bremsstrahlung contributed; thus the expected brightness temperatures represented the *minimum* possible microwave intensities from the soft X-ray sources.

More recent coronal elemental abundance determinations (Meyer 1991, 1992; Feldman et al. 1992; Reames 1993) indicate that coronal abundances of elements with low first ionization potential (FIP) are actually *enhanced* by factors of 3.5–4 relative to the earlier tabulated values. This leads to reduced column emission measures relative to the earlier values, which in turn leads to lower expected free-free brightness temperatures. We have recalculated the expected 1.5 GHz brightness temperatures for selected lines of sight (those for which tabular data are presented in the above CoMStOC references) in the four CoMStOC cases using factor of 4 enhanced coronal elemental abundances and found that in all but one case the expected brightness temperatures still exceed the observed by factors ~ 2. Thus the requirement for cool coronal plasma is not obviated by factor of 4 decrements in the column emission measure. We also reexamined the observations of Webb et al. (1987) and found the same result: cool coronal plasma is still required to explain those data.

We also revisited the plage area observed with SERTS and the VLA by Brosius et al. (1993). Those authors, using the revised Meyer (1991; 1992, private communication) coronal iron abundance (other elements did not enter into the computations), found excellent agreement between the expected and the observed 1.5 GHz observations. This led them to conclude that thermal bremsstrahlung alone was sufficient to produce the observed microwave emission. If a lower (by a factor of 4, as in Meyer 1985) coronal iron abundance is assumed, however, the expected brightness temperature exceeds the observed by a factor ~ 4. This indicates, as with the CoMStOC observations, that cool coronal plasma must lie along the line of sight between the observer and the EUV/microwave source. In this case, however, conclusions regarding the presence or absence of cool coronal plasma depend upon the choice of coronal iron abundance. This demonstrates that significant changes can result from uncertainties in determinations of coronal elemental abundances (see Saba & Strong 1994).

For the present work, we also investigated effects of coronal elemental abundance reductions by a factor of 4 from the Feldman et al. (1992) values that we used above by increasing the averaged active region DEM uniformly by a factor of 4. Then, averaged over the entire active region image shown in Figure 1, the expected 1.5 GHz intensity exceeds the observed by a factor of 2.1. In roughly two-thirds of the pixels the expected intensity exceeds the observed by a factor of 1.7, the differences being smallest toward the interior, brightest parts of the region. At locations (1) and (2) (the 6 and 20 cm peaks, respectively) the expected values exceed the observed L and R values by factors between 1.2 and 1.4; in light of possible measurement uncertainties, such differences may not be significant, implying that free-free emission alone would be sufficient to account for the observed microwave intensities at these two locations in the case of decreased coronal abundances. However, at location (3) the expected brightness temperature would then exceed the observed by a factor ~ 2, indicating a need for cool absorbing coronal plasma. (Indeed, for other locations in the outskirts of the region, the expected brightness temperature would exceed the observed by factors between 2 and 6.) In that case gyroemission may not be required to explain the observed microwave emission, and the resulting coronal magnetic field may be different from what we derived above. Therefore, the variation in coronal abundance that we have assumed would not only change our conclusion regarding the absence of cool coronal plasma, but also affect our calculated coronal magnetic field strengths. Since the Meyer (1991, 1992, private communication), Feldman et al. (1992), and Reames (1993) values are currently generally accepted as providing the most reliable coronal elemental abundances, we do not repeat our coronal magnetography computations using the older (Meyer 1985) abundances. As was pointed out by Saba & Strong (1994), coronal abundance uncertainties and variations can seriously complicate the analysis and interpretation of solar observations.

We characterize the temperature distribution of the emitting plasma with the SERTS DEM in the present work. This is a more realistic approach than the isothermal approximation (imposed by the paucity of available X-ray emission lines) that was used for CoMStOC since the coronal temperature is known to vary with height along any given line of sight. The DEM was derived with numerous emission lines from various ionization stages of Fe, Ne, Mg, Si, and Ni using the equilibrium ionization computations of Monsignori-Fossi (1992) (which include the Arnaud & Raymond 1992 tabulations for iron). Because the density- and temperature-insensitive line intensity ratios of the emission lines from these ions all yield close agreement with their respective theoretical values (Brosius et al. 1996), the accuracy of the atomic physics parameters and the equilibrium ionization fractions used in the present work is confirmed.

We investigated the possibility that the Arnaud & Rothenflug (1985) equilibrium ionization fractions used for the CoMStOC analyses may have introduced uncertainties in the CoMStOC results. The means by which these computations would introduce their largest uncertainties is in the derivation of the column emission measure. Since the CoMStOC column emission measure maps were derived from the calculated temperature maps (which are less sensitive to uncertainties in the equilibrium ionization fractions than the emission measure maps) and the O VIII intensity images, uncertainties in the O VIII equilibrium ionization fractions could significantly affect the CoMStOC results. We compared the O VIII fractional abundances of Arnaud &

Rothenflug (1985) with those of Monsignori-Fossi (1992), and found only small differences at the ionization peak (log $T_{max} \sim 6.3$–6.4), with differences approaching factors of 2 far from the peak. The agreement between these two tabulations suggests that the O VIII equilibrium ion abundances are fairly well determined and are not expected to harbor factor of 2 or more uncertainties, especially at the ionization peak. Thus we find no differences between the available ionization computations which would eliminate the need for cool coronal plasma in the CoMStOC observations.

It should be mentioned that, although we find no evidence for the presence of a "quasi-transverse" layer in the coronal magnetic field based on a comparison between the observed and the calculated microwave emission when the Feldman et al. (1992) coronal elemental abundances are used, the potential extrapolation yields such a layer above the active region. Although it is beyond the scope of the present analysis, it would be interesting to see how that layer would correspond with areas in which microwave polarization inversion is required after absorption by cool coronal plasma reduces the calculated microwave brigtness temperatures to the observed values (as in Brosius et al. 1991, 1992; Schmelz et al. 1992) when the older (Meyer 1985) coronal elemental abundances are used. The presence of the QT layer in the extrapolated potential field is somewhat bothersome, particularly in the absence of a need for polarization inversion. However, in light of the differences between the potential coronal fields and our derived coronal fields it is possible that coronal electric currents may alter the potential configuration sufficiently so as to eliminate the QT layer. Alternatively, it is possible that a QT layer does in fact overlie the active region but that the electron density in that layer is appropriate for strong (rather than weak) mode coupling, so that polarization inversion would not occur. Additional observations would, of course, be useful to help resolve and generalize this issue.

6. CONCLUSIONS

We summarize our conclusions as follows, based on our use of the Feldman et al. (1992) coronal elemental abundances:

1.—Thermal bremsstrahlung emission alone is not sufficient to produce the observed microwave intensities from NOAA region 7563: gyroemission is also required.

2.—There is no evidence for cool, absorbing plasma in the solar corona above region 7563.

3.—We successfully obtained a three-dimensional coronal magnetic field which yields the observed microwave intensities at the two different analyzed frequencies of 1.465 and 5.0 GHz (20 and 6 cm wavelengths).

4.—Extrapolated potential fields at heights of ~5000–16,000 km are typically factors ~2 or more smaller than the coronal fields derived with our method. The difference is smaller in the small sunspot from which the 6 cm intensity peak originates. This suggests that the sunspot magnetic field is nearly potential but that coronal electric currents play a significant role elsewhere in the active region.

5.—Although we cannot firmly establish the uniqueness of our solution in this particular case, our method is a powerful one and should be repeated with other similar data sets. The coronal magnetic field could be better constrained if data from additional radio observing frequencies were available.

6.—Our method could be improved if we had density diagnostics available over a wider temperature range; this would eliminate or reduce the need to extrapolate the density as a function of temperature, and it would provide more information on the volume filling factor so that an adequate height scale could be derived.

J. W. B. acknowledges NASA support through contracts NASW-4933 and NASW-5020. J. M. D. and R. J. T. acknowledge NASA support for the SERTS program by RTOP grants from the Solar Physics Office of NASA's Space Physics Division. NSO/Kitt Peak data used here are produced cooperatively by NSF/NOAO, NASA/GSFC, and NOAA/SEL. Solar radiophysics at the University of Maryland is supported by NSF grant ATM 93-16972 and NASA grant NAG-W-1541.

REFERENCES

Arnaud, M., & Raymond, J. 1992, ApJ, 398, 394
Arnaud, M., & Rothenflug, R. 1985, A&AS, 60, 425
Bandiera, R. 1982, A&A, 112, 52
Bastian, T. S. 1994, ApJ, 426, 774
Bogod, V. M., Gelfreikh, G. B., Willson, R. F., Lang, K. R., Opeikina, L. V., Shatilov, V., & Tsvetkov, S. V. 1992, Sol. Phys., 141, 303
Brosius, J. W., Davila, J. M., Thomas, R. J., & Monsignori-Fossi, B. C. 1996, ApJS, 106, 143
Brosius, J. W., Davila, J. M., Thomas, R. J., Saba, J. L. R., Hara, H., & Monsignori-Fossi, B. C. 1997, ApJ, 477, 969
Brosius, J. W., Davila, J. M., Thompson, W. T., Thomas, R. J., Holman, G. D., Gopalswamy, N., White, S. M., Kundu, M. R., & Jones, H. P. 1993, ApJ, 411, 410
Brosius, J. W., Holman, G. D., & Schmelz, J. T. 1991, Eos, 72, 449
Brosius, J. W., Willson, R. F., Holman, G. D., & Schmelz, J. T. 1992, ApJ, 386, 347
Falconer, D. A. 1994, Ph.D. thesis, Univ. Maryland
Feldman, U., Mandelbaum, P., Seely, J. F., Doschek, G. A., & Gursky, H. 1992, ApJS, 81, 387
Gary, D. E., & Hurford, G. J. 1994, ApJ, 420, 903
Ginzburg, V. L. 1964, Propagation of Electromagnetic Waves in Plasma (New York: Gordon & Breach)
Holman, G. D. 1986, in Coronal and Prominence Plasmas, ed. A. I. Poland (NASA CP-2442), 297
Jones, H. P., Duvall, T. L., Jr., Harvey, J. W., Mahaffey, C. T., Schwitters, J. D., & Simmons, J. E. 1992, Sol. Phys., 139, 211
Kanno, M., & Suematsu, Y. 1982, PASJ, 34, 449
Kundu, M. R., Schmahl, E. J., & Gerassimenko, M. 1980, A&A, 82, 265
Kundu, M. R., Schmahl, E. J., & Rao, A. P. 1981, A&A, 94, 72
Lang, K. R., et al. 1993, ApJ, 419, 398
Lang, K. R., Willson, R. F., Smith, K. L., & Strong, K. T. 1987a, ApJ, 322, 1035
———. 1987b, ApJ, 322, 1044
Lee, J., White, S. M., Gopalswamy, N., & Kundu, M. R. 1997, Sol. Phys., in press
Meyer, J.-P. 1985, ApJS, 57, 173
———. 1991, Adv. Space Res., 11, 269
Monsignori-Fossi, B. C. 1992, unpublished
Monsignori-Fossi, B. C., & Landini, M. 1991, in Intensity Integral Inversion Techniques: a Study in Preparation for the *SOHO* Mission, ed. R. A. Harrison & A. M. Thompson (RAL-91-092), 27
———. 1995, in IAU Colloq. 152, ed. S. Bowyer & B. Haisch, 543
Neupert, W. M., Epstein, G. L., Thomas, R. J., & Thompson, W. T. 1992, Sol. Phys., 137, 87
Nitta, N., White, S. M., Kundu, M. R., Gopalswamy, N., Holman, G. D., Brosius, J. W., Schmelz, J. T., Saba, J. L. R., & Strong, K. T. 1991, ApJ, 374, 374
Pallavicini, R., Sakurai, T., & Vaiana, G. S., 1981, A&A, 98, 316
Ramaty, R. 1969, ApJ, 158, 753
Reames, D. V. 1993, Adv. Space Res., 13, 339
Saba, J. L. R., & Strong, K. T. 1994, in Proc. Kofu Symp., NRO Rep. No. 360, 305
Sakurai, T. 1982, Sol. Phys., 76, 301
Schmahl, E. J., & Orrall, F. Q. 1979, ApJ, 231, L41
Schmelz, J. T., Holman, G. D., Brosius, J. W., & Gonzalez, R. D. 1992, ApJ, 399, 733

Schmelz, J. T., Holman, G. D., Brosius, J. W., & Willson, R. F. 1994, ApJ, 434, 786
Shibasaki, K., Chiuderi-Drago, F., Melozzi, M., Slottje, C., & Antonucci, E. 1983, Sol. Phys., 89, 307
Webb, D. F. 1981, in Solar Active Regions, ed. F. Q. Orrall (Boulder: Colorado Assoc. Univ. Press), p. 165
Webb, D. F., Davis, J. M., Kundu, M. R., & Velusamy, T. 1983, Sol. Phys., 85, 267
Webb, D. F., Holman, G. D., Davis, J. M., Kundu, M. R., & Shevgaonkar, R. K. 1987, ApJ, 315, 716
White, S. M., Gary, D. E., & Kundu, M. R. 1996, BAAS, 28, 956
White, S. M., & Kundu, M. R. 1997, Sol. Phys., in press
Zheleznyakov, V. V. 1970, Radio Emission of the Sun and Planets, ed. J. S. Hey (Oxford: Pergamon)
Zirin, H., Baumert, B. M., & Hurford, G. J. 1991, ApJ, 370, 779